

We are IntechOpen, the world's leading publisher of Open Access books Built by scientists, for scientists

6,900

Open access books available

186,000

International authors and editors

200M

Downloads

Our authors are among the

154

Countries delivered to

TOP 1%

most cited scientists

12.2%

Contributors from top 500 universities



WEB OF SCIENCE™

Selection of our books indexed in the Book Citation Index
in Web of Science™ Core Collection (BKCI)

Interested in publishing with us?
Contact book.department@intechopen.com

Numbers displayed above are based on latest data collected.
For more information visit www.intechopen.com



Radiometric Mapping of Hydrothermal Alterations in Isla Isabel, Mexico

Román Alvarez and Gerardo Figueroa

Abstract

Isla Isabel is a small island of volcanic origin about 29 km west of Nayarit's coast, Mexico, exhibiting phreatomagmatic activity (maars). In a nearby (8 km), ocean located, exploration well reaching 3157 m geothermal gradients of 73°C/km were recorded, which are among the largest in the world. These features, plus gravimetric anomalies in the area, suggest that the region may become an important source of geothermal energy. Direct hydrothermal alteration mapping in the island is difficult since it is a National Park and a bird sanctuary where various bird species thrive. We used remote sensing techniques to identify hydrothermally altered sections in the island, including radiometric spectrum determinations in the 350–1050 nm wavelength interval and Landsat 8 satellite imagery. The island is mainly composed of basalt but large portions contain vegetation, posing a challenge to satellite hydrothermal alteration detection. Four pixel-classification schemes are used for oxides, hydroxyls, and vegetation; shallow underwater basalt flow detection was possible.

Keywords: Isla Isabel, Mexico, hydrothermal alteration, phreatomagmatic activity, oxide and hydroxyl detection, radiometric spectra

1. Introduction

Isla Isabel is an island of volcanic origin located ~29 km west of the coast of Nayarit State and ~70 km east of Islas Tres Marias archipelago in the Mexican Pacific; its geographic location is 21°50.847'N, 105°53.000'W (**Figures 1** and **2**). The geologic composition of the island is basaltic with various explosion craters (maars) of Surtseyan (phreatomagmatic) origin scattered in the surface [1]. The island dimensions are 1.8 km N-S and 1.32 km E-W.

A regional study around Isla Isabel showed that the island represents the emerged portion of a larger body preliminarily identified as a laccolith [2]. Over the average depth of 100 m of the continental platform in which the island is located, a topographic bulge rises to the surface; its dimensions are 20 km in the NW-SE direction and 17 km in the perpendicular direction. This bulge has been assumed to be built by successive magmatic intrusions that are deflected sideways by the sediments; the island represents the only emerged portion of this laccolith. In addition to the regional study, local geophysical surveys have been made on the emerged portion. Interpretation of magnetic and gravity results on the island's surface suggests the existence of diatremes associated with some of the explosion craters, as well as identification of a growth boundary about 800 m deep, from which apparently originated

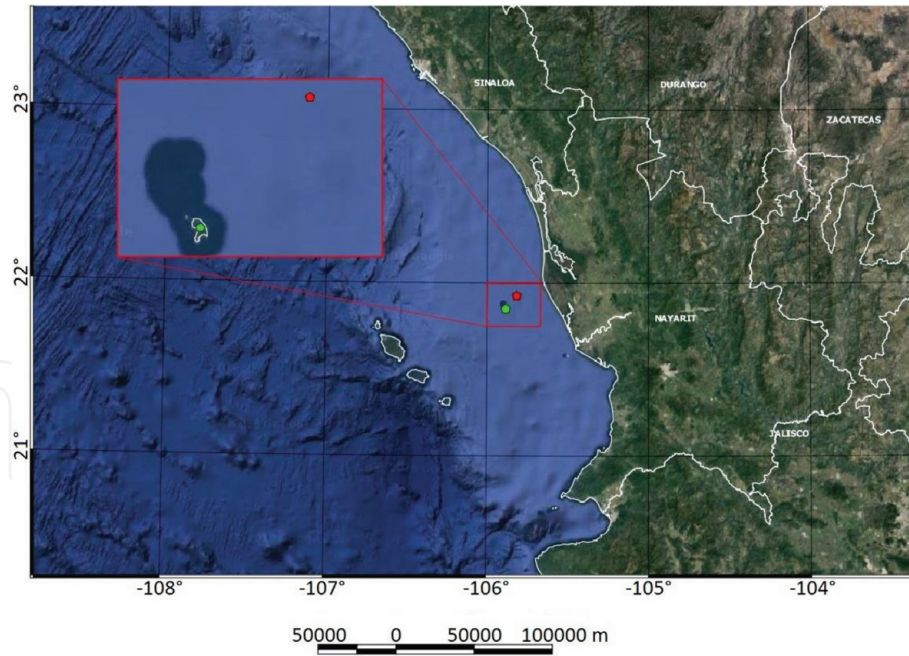


Figure 1. Location of Isla Isabel (green dot) and exploration well Huichol I (red dot). Tres Marias islands are located SW of Isla Isabel.

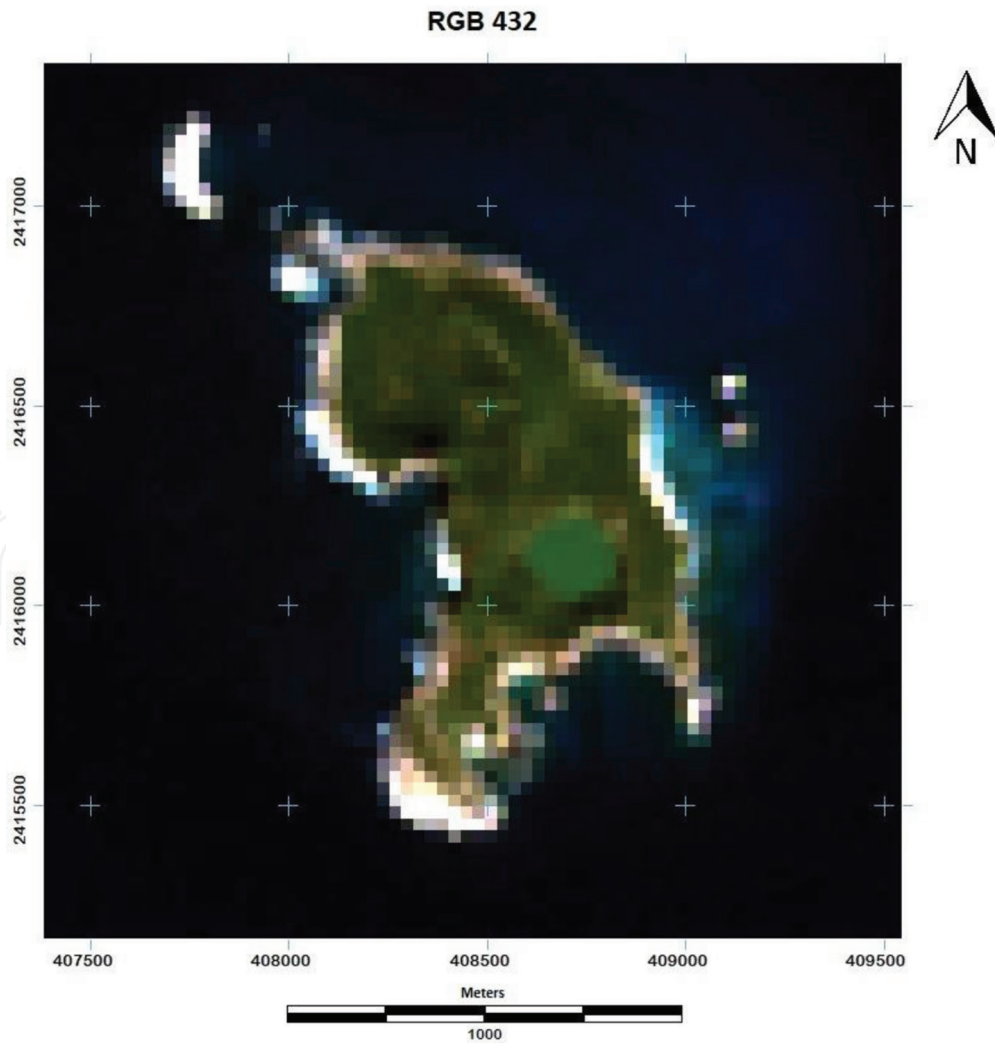


Figure 2. Landsat 8 image Path/Row 31/45, code LC80310452014002LGN00 obtained on February 13, 2014. The image (RGB composite 4-3-2) is shown after image crop out, and atmospheric and radiometric corrections were made. Spatial resolution is 30 m. The fuzzy appearance is due to the scale used, which begins to show individual pixels.

one of the latest constructional, basaltic episodes [3]. Alkali basalts have transported mafic and ultramafic peridotite xenoliths to the surface; sequences of dark-red, near-vent scoria deposits, and lava flows in the tidal zone have also been reported [1].

Huichol I exploration well was drilled about 8 km NE of the island (**Figure 1**) penetrating 3157 m, with diabase intersected in the deepest 250 m. Geothermal gradients reached the values of 73°C/km, some of the largest measured in the world [4], highlighting the anomalously high heat flux in the area.

The above observations suggest that the island and its surroundings deserve geological and geophysical studies to evaluate its geothermal potential. In the present study, we focus on hydrothermal alteration detection and mapping in the island, with remote sensing techniques.

2. Radiometric spectra

The radiometric aspects of the island materials are approached from direct spectrum determinations with a radiometer and from the numerical analysis of the selected Landsat 8 image. To obtain the reflectance of the sampled surfaces, we used an Ocean Optics USB2000+VIS+NIR radiometer with a bandwidth ranging from 350 to 1050 nm. These reflectances are then compared to those of the corresponding bands of the Landsat 8 image. The rocks measured radiometrically were analyzed by X-ray fluorescence obtaining their elemental compositions, which also allowed for comparison with the spectral signature of the corresponding database of the US Geological Survey [5].

Landsat 8 images have 11 bands; of them, we used coastal/aerosol, blue, green, red, Near Infra-Red (NIR), and the 2 Short Wavelength Infra-Red (SWIR) bands. The atmospheric correction was performed with the Histogram Minimum Method [6], and resampling of the digital numbers was made to fit into the 8-bit radiometric resolution format. The spatial resolution was not changed. **Figure 2** shows a color composition (RGB-432) of the image after preprocessing was accomplished. At this scale, the individual pixels of 30 × 30 m begin to show, giving the image a fuzzy appearance.

2.1 Radiometric stations

Ten stations were sampled across the island; at each station, several radiometric measurements were made, and rock samples were collected for subsequent composition analyses. **Figure 3** shows the location of each station and **Table 1** summarizes pertinent information. Owing to space reasons, data obtained in some stations will be omitted in this report.

2.1.1 Station 1

This station corresponds to a basalt outcrop, and the reflectance spectra are shown in **Figure 4**. The four curves follow the same tendencies, with the same variations in percentage reflectance, indicating a consistent response at the station. The different reflectance baselines are attributed to different collection angles. Reflectance is fairly low in Station 1; the four spectra show a wide maximum between 440 and 640 nm.

2.1.2 Station 2

This station contains two different lithological units. The first is a basalt outcrop, and the second corresponds to white pumice. **Figure 5** shows the outcrops and the

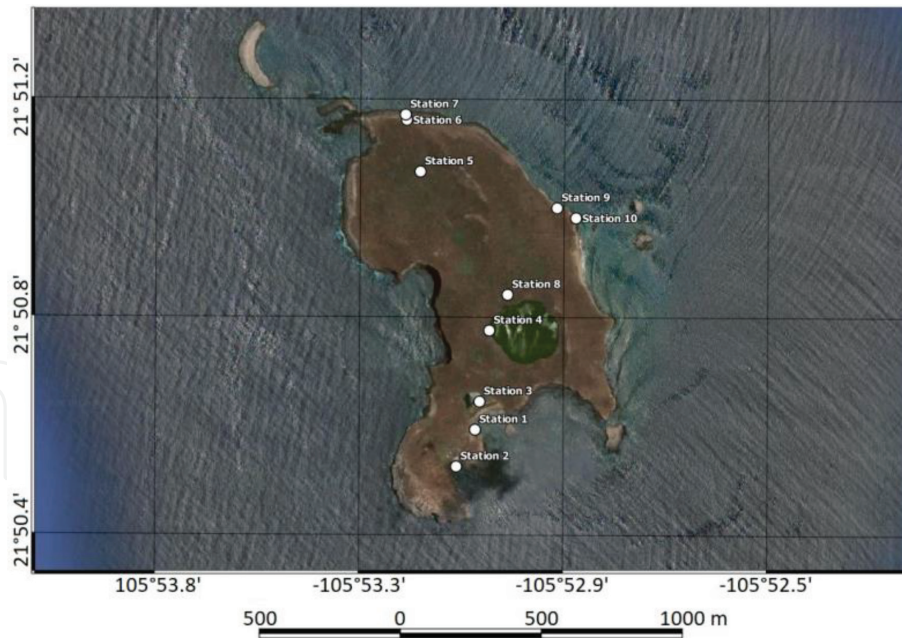


Figure 3. Image of Isla Isabel composed of Google Earth images from June 23, 2015. The location of the radiometric stations corresponds to the white dots.

Station	Easting	Northing	Samples	Type
1	408,543	2,415,752	4	Basalt
2-1	408,476	2,415,621	4	Basalt
2-2			2	White tuff
3-1	408,558	2,415,852	4	Soil
3-2			4	Vegetation
4-1	408,594	2,416,106	4	Basalt
4-2			2	Basalt
5	408,349	2,416,672	1	Basalt
6	408,302	2,416,856	1	Basalt
7	408,298	2,416,874	4	Basalt
8	408,659	2,416,232	3	Vegetation
9	408,659	2,416,540	3	Basalt
10-1	408,834	2,416,505	3	Tuff
10-2	408,659	2,416,232	3	Basalt

Table 1. Station location in UTM coordinates, number of spectral samples, and corresponding rock type.

measuring equipment, and **Figures 6** and **7** show the radiometric responses of basalt and the white tuff. As in Station 1, the basalt exhibits consistent radiometric responses in the four determinations. However, the response differs slightly from that of basalts in Station 1, since they show a plateau between 500 and 600 nm, where the former showed a broad reflectance peak.

The white pumice, as expected, shows radically different spectra from that of basalt. These determinations also show consistency between them, being characterized by a monotonous increase in reflectivity between 360 and 700 nm which evoke the response of a dry, bare soil followed by rapid variations at the end of the spectrum.

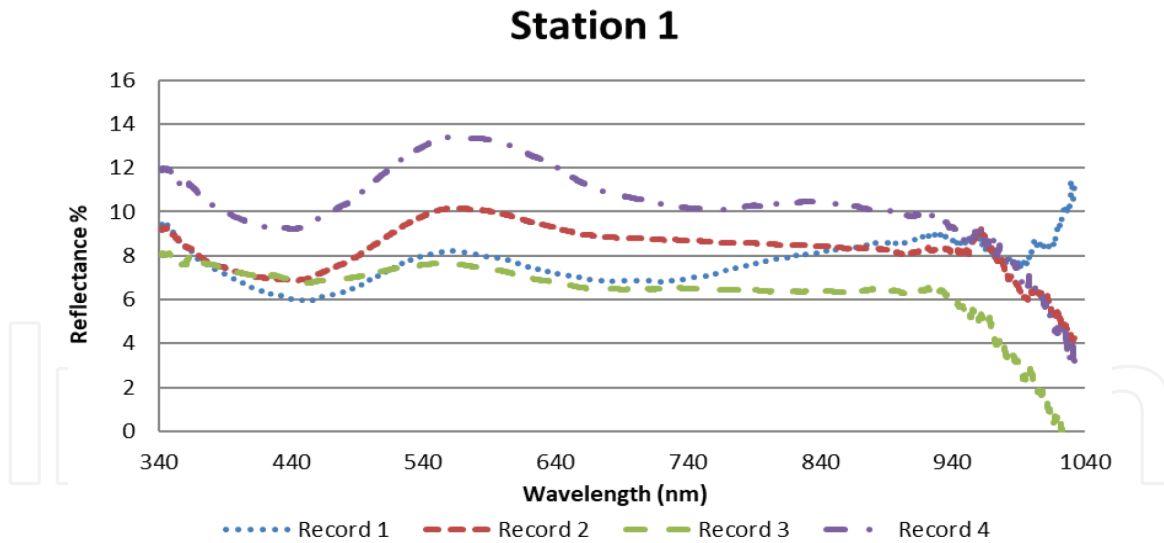


Figure 4.
Four radiometric records obtained at Station 1 in Isla Isabel. The station location is shown in **Figure 3**, and its coordinates appear in **Table 1**. The rock composition corresponds to basalt.



Figure 5.
Measuring basalt with the spectrometer; the PC control and record measurements. At Station 2, two types of materials were sampled: Basalt and white tuff.

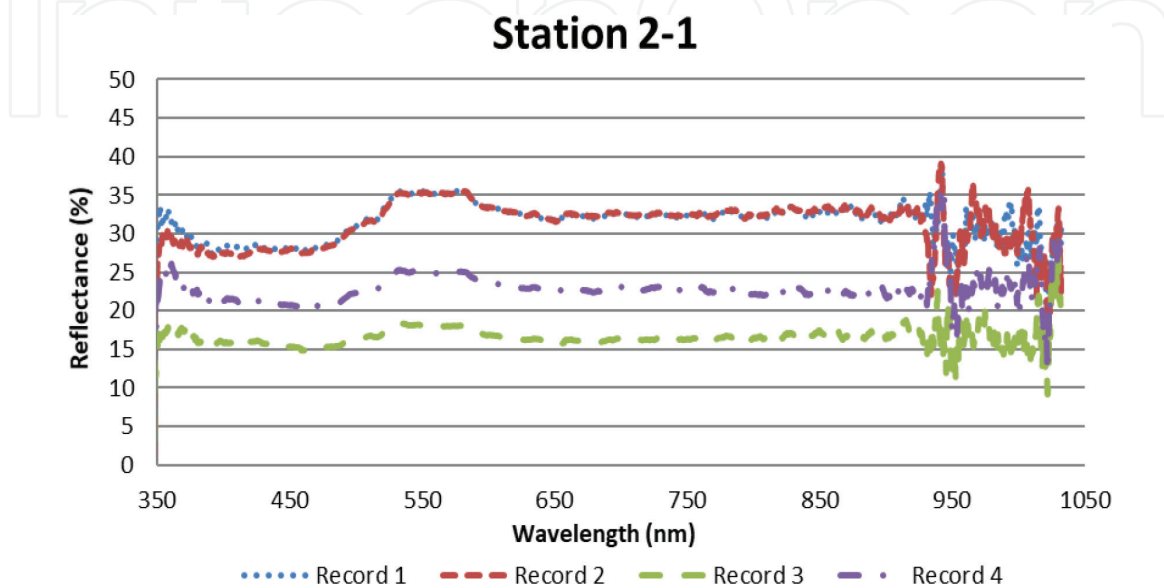


Figure 6.
Four records of the radiometric response of basalt at Station 2-1.

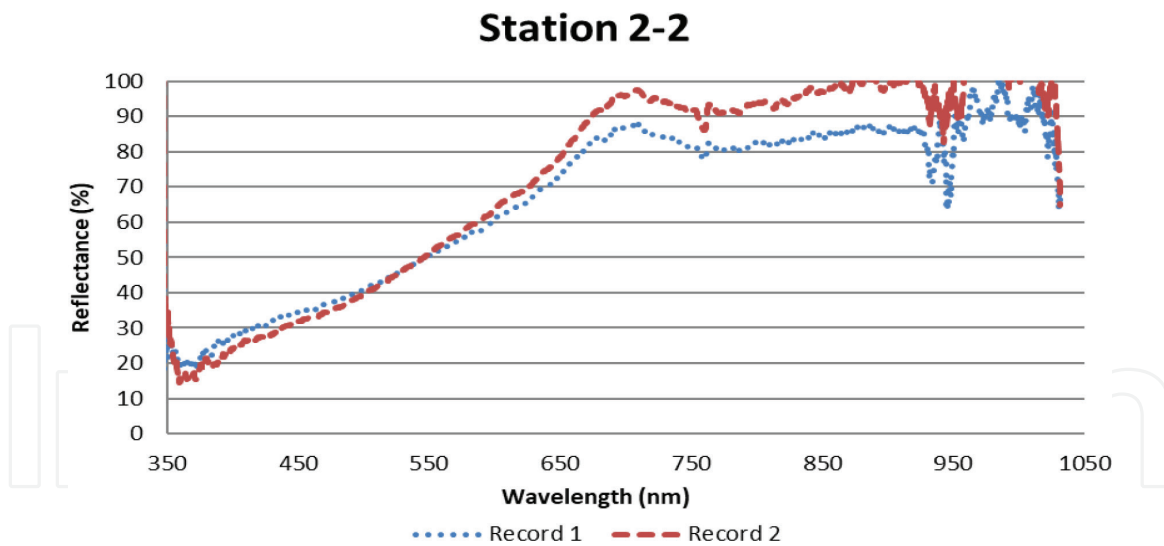


Figure 7.
Radiometric response of white pumice at Station 2-2.

2.1.3 Station 4

This station is located on the margin of Lago Crater (also known as Laguna Fragatas) as shown in **Figure 3**; according to [1], this structure is the only, fully preserved, explosion crater in the island. The exposed rocks on the lake's margin are basalts altered either by the fluctuating water level (**Figure 8**) or by the chemical action of birds' excrement. The latter mechanism appears more viable since birds are abundant in the island; Islote Pelon, slightly north of the island, is an extreme case of these alterations, being completely covered by bird feces. The white surfaces of the rocks induced saturation in the radiometer making it difficult to obtain valid readings. The spectra from Station 4-1, shown in **Figure 11**, were obtained pointing to dark spots of the chemically altered rock samples. We observed a systematic tendency for reflectance to diminish as the wavelength increases; the large reflectance contribution to the lower part of the spectrum probably arises in dispersed radiation at the white surfaces of the rocks as well as at the lake's surface.

Although distorted by the dispersion effect, two of the signatures clearly show a similar increment in reflectance between 500 and 600 nm as those shown by basalt



Figure 8.
Chemically altered basalts on the margin of Lago Crater. We attribute this alteration to the chemical effect of bird feces.

in Station 1 and Station 2-1. Between 690 and 900 nm, it also shows the vegetation signature, compare to that of Station 8 (**Figure 12**).

2.1.4 Station 5

This station is in a bushy area where vegetation height ranges between 2 and 3 m. Many birds nest in the area, and the outcropping rocks have been exposed to their excrements during long periods. The surface of the sample chosen for the measurement was under such conditions. In **Figure 9**, a hand specimen from the same outcrop is shown; its exterior is chemically altered, while its interior shows the dark color of unaltered basalt. The radiometric response is shown in **Figure 10**. Reflectance is flat from 450 to 700 nm and quite similar to the response of the altered surface at Station 4-1, Record 1 (**Figure 11**) in the same interval.



Figure 9. Basalt hand specimen collected at Station 5. The white surface has been exposed and chemically altered, while the fresh portion appears black.

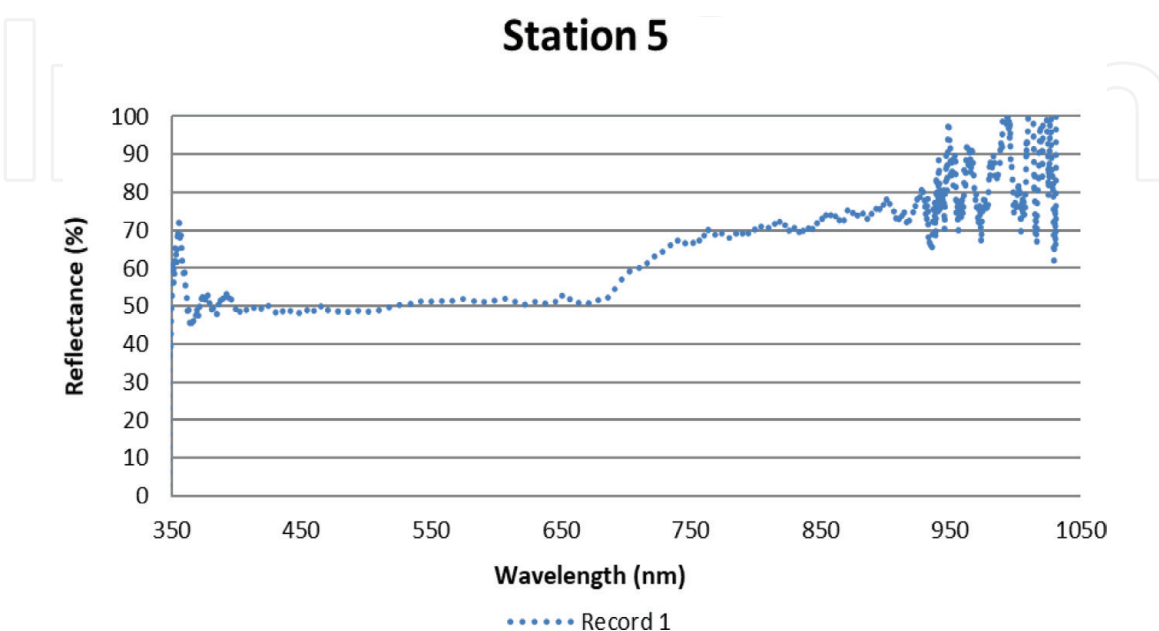


Figure 10. Radiometric response at Station 5. A combination of shade and chemically altered surface may correspond to the flat response between 400 and 700 nm. The reflectance increment between 700 and 950 nm is attributed to the effect of vegetation surrounding the station.

Station 4-1

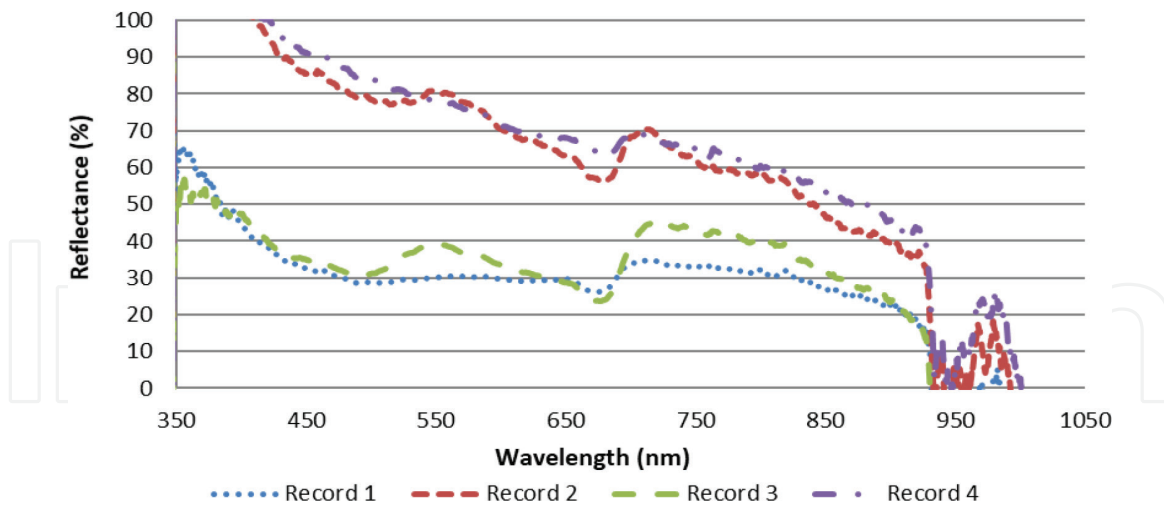


Figure 11. Spectral signature of chemically altered basalt in the shore of Lago Crater. It was obtained pointing to the darker portions of the rock. Reflectance increase in the lower part of the spectrum is attributed to dispersion effects.

Although no direct testing for the effects of bird’s feces on basalt is available, bird droppings are known to chemically alter hard surfaces such as concrete [7]. These authors analyzed samples of concrete using scanning electron microscopy for morphological properties and X-ray spectrophotometry for surface elements, finding that the components of bird excrement penetrate microcracks causing it to become smoother. They also found that concrete materials exposed to bird feces lost weight more than the control samples.

2.1.5 Station 8

This station is located on the rim of Lago Crater; the interest here was to obtain a clean vegetation record from the top of the rim. Three records are shown in **Figure 12**; they neatly show the radiometric signature of vegetation, with a reflectance peak centered at 550 nm and a large reflectance in the 700–950 nm NIR region, typical of healthy vegetation [8]. The records differ in percent reflectance but basically maintain the same

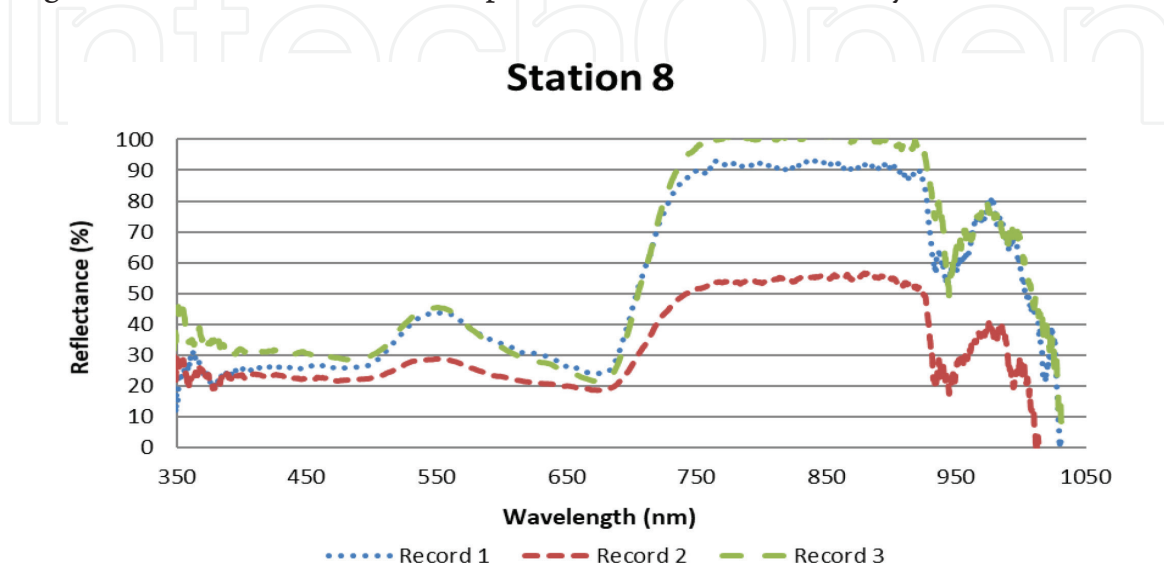


Figure 12. Station 8 is located on the top of the north rim of Lago Crater. The objective was to obtain the radiometric signature of vegetation around the crater.

spectral signature. The reflectance peaks centered at 550–980 nm are well defined and differ from the response of the geologic materials obtained in other stations.

2.1.6 Station 9

Located on the eastern portion of the island, and this station corresponds to basalt without chemical alteration. Notice the low reflectance values (**Figure 13**), indicating the strong absorption of this rock. The larger reflectance noted in previous basalt samples in the 500–600 nm range is also present here, although somewhat subdued by the strong absorption. The rapid variations in the NIR range show large amplitudes in the three records.

2.1.7 Station 10-2

This station corresponds to basalt not affected by chemical alteration. The records are shown in **Figure 14**, they show coherency among themselves, although Record 1 shows an anomalously high baseline reflectance, which we attribute to calibration effects. Record 1 shows rather high levels of reflectance with a well-defined plateau between 500 and 600 nm, as previously noted for other basalt samples. This feature is also present, although somewhat subdued, in Records 2 and 3. Between 350 and 500 nm, the latter shows a monotonous decrease in reflectivity that is not present in Record 1; they are attributed to the dispersion effect previously observed in other samples in this study. The NIR responses of the three records are quite similar and show various localized radiation absorptions.

2.1.8 Summary

Summarizing these radiometric results, we conclude that basalts present a distinct signature throughout the island, showing low reflectance, usually below 20%, that is distorted in some stations by alterations and/or the influence of disperse radiation. The calibration procedure performed prior to each measurement, and

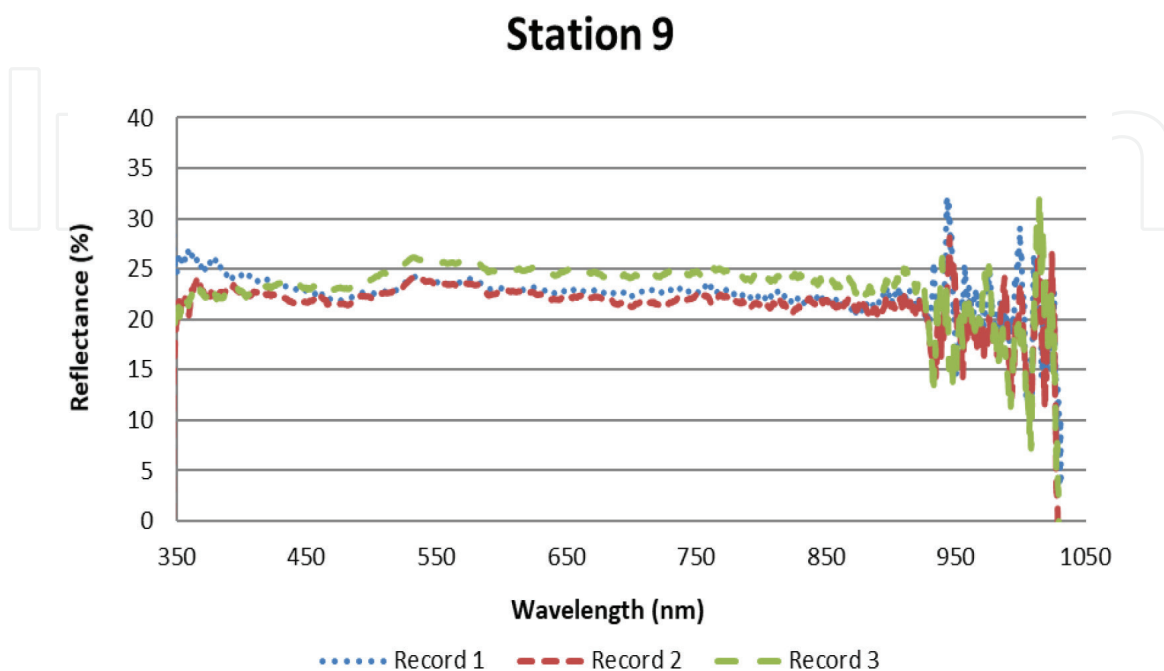


Figure 13. Station 9 is located on the eastern portion of the island where unaltered basalts are clearly exposed. This station and Station 1 showed the lowest reflectance values in the island.

Station 10-2

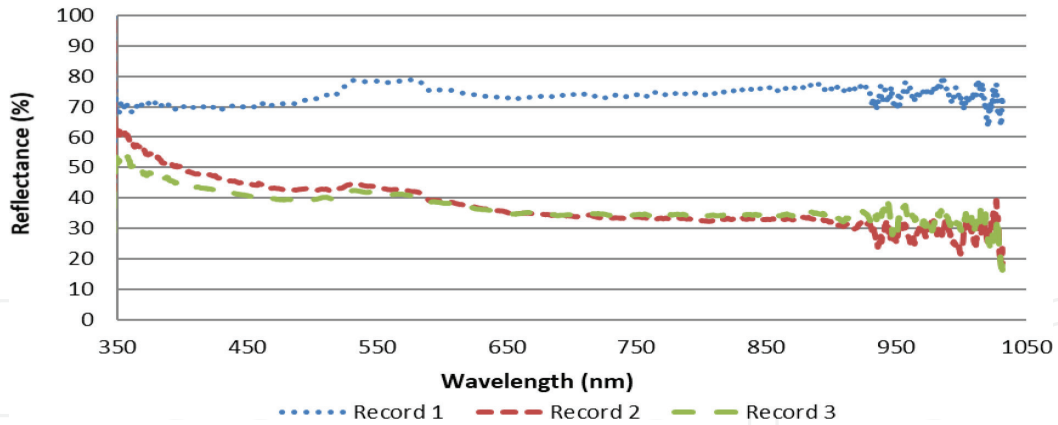


Figure 14. Radiometric signatures of basalt at Station 10-2. These basalts did not present signs of chemical alteration. The baselines show larger values than those previously observed in basalt.

the angle of measurement are most likely responsible for the baseline variations between measurements. Without considering the NIR band, we can establish a plateau reflectance response in the 500–600 nm bandwidth followed by a flat region between 650 and 900 nm, as the characteristics of the basalt response in this group of measurements (Figures 4, 6, 7, and 14).

3. Comparison of satellite and radiometric data

To better evaluate the type of radiometric departures between in situ measurements, which sample small, specific locations at an observation station, and satellite determinations which necessarily involve averaging the radiometric responses of the various materials in each pixel, we performed a comparison between them. We used the least noisy spectrum for each station as well as the values of the Landsat 8 pixel that contains the corresponding station, obtaining the values of the digital numbers of each band: B1, B2, B3, B4, and B5; these values were converted to a 0–100% reflectance scale and plotted with the corresponding spectral signature (Figures 15–17). The SWIR bands do not overlap the radiometer’s range.

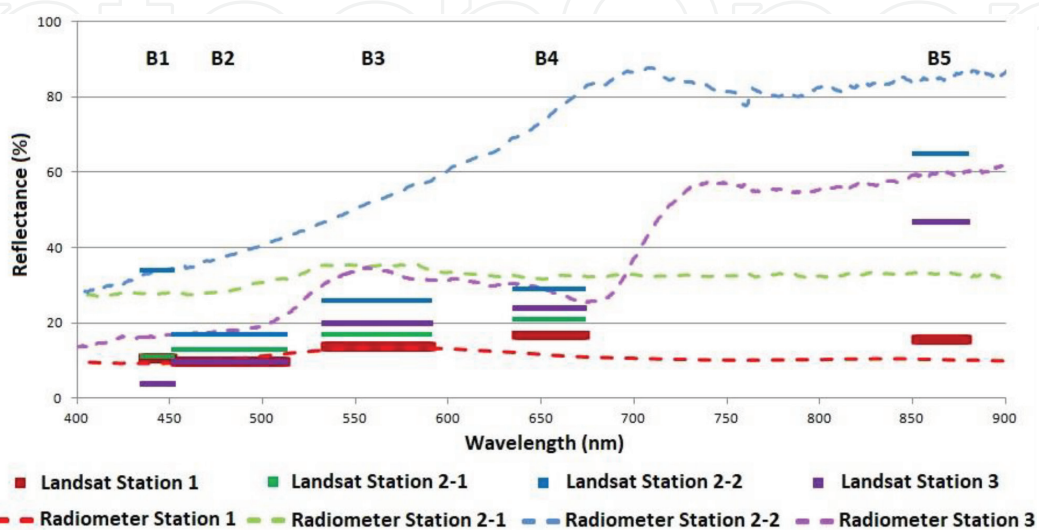


Figure 15. Reflectance comparison between Landsat 8 pixels and radiometric stations. Stations 1, 2-1, 2-2, and 3. The band coverage is shown as colored, continuous lines, while dashed lines correspond to the radiometric determinations.

In **Figure 15**, the low reflectance obtained with the radiometer in Station 1 corresponds well with the values obtained from the pixel of the Landsat 8 image. In Station 2-2, the radiometer readings overshoot those of Landsat 8 but maintain the general trend. Stations 2-1 and 3 correspond well with the satellite radiometric responses. In **Figure 16**, Station 4 departs considerably from the satellite band behavior. Although Stations 5, 6, and 7 conform to the general trends of the satellite measurements, reflectance is considerably larger.

In **Figure 17**, radiometric Stations 8, 9, and 10-2 show a behavior similar to the Landsat 8 bands, although displaced and amplified. Station 10-1 departs from the satellite bands owing mostly to the dispersion effect clearly shown below 700 nm.

We conclude that there is a fair agreement between the satellite and the in situ measurements. With the ground truth of the radiometric stations, we can now proceed to analyze the satellite data.

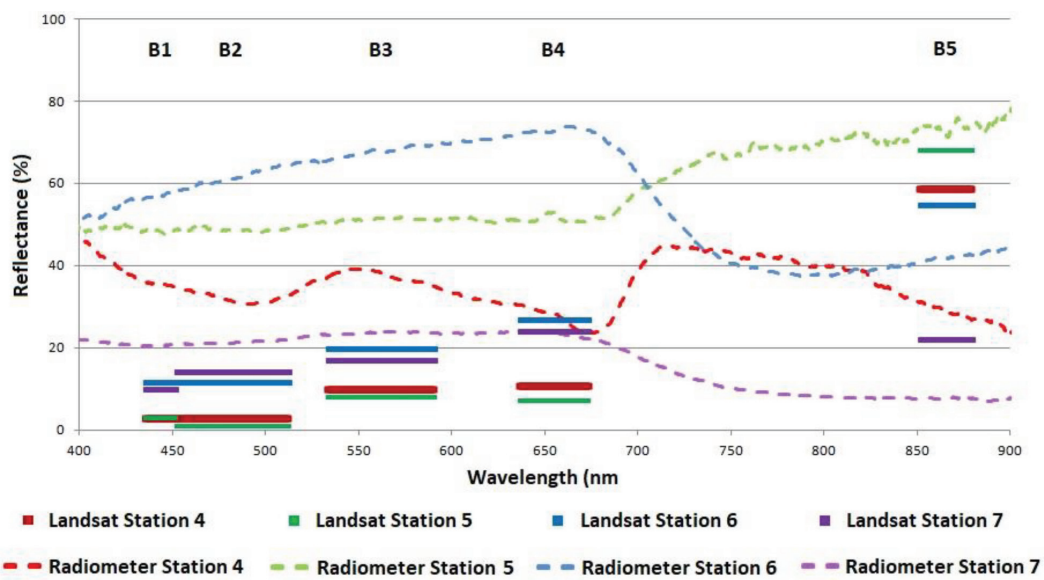


Figure 16.
 Reflectance comparison between Landsat 8 pixels and radiometric stations. Stations 4, 5, 6, and 7.

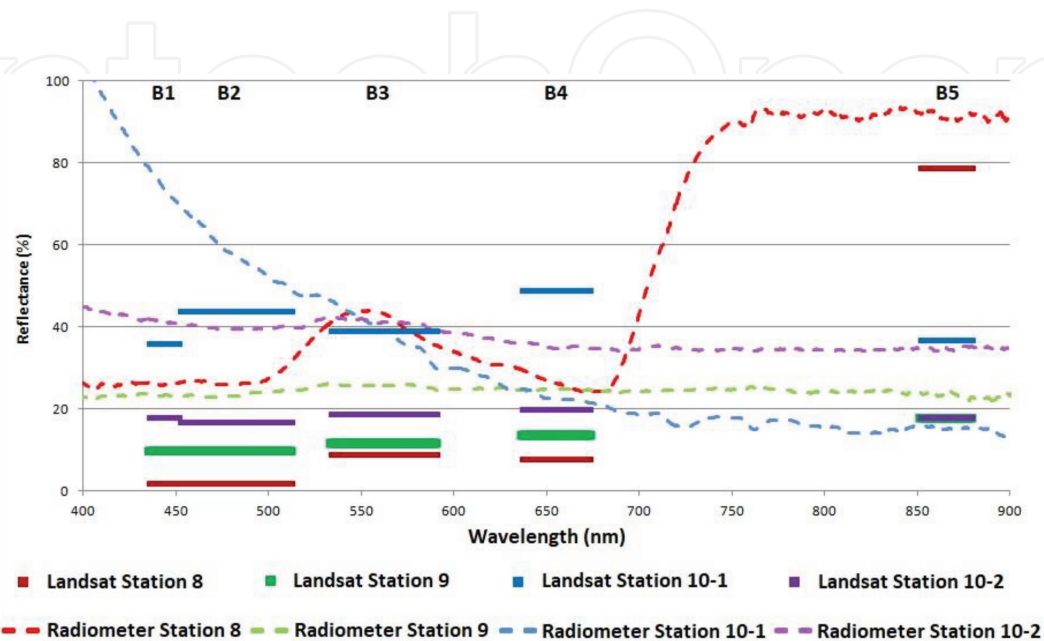


Figure 17.
 Reflectance comparison between Landsat 8 pixels and radiometric stations. Stations 8, 9, 10-1, and 10-2.

4. Geochemistry

To properly associate radiometric response to rock composition, we need to perform a geochemical analysis on the samples where reflectance was measured, particularly on those identified as basalts, since they are the most common. Ten geochemical analyses throughout the island have been published [1]; we deemed sufficient to analyze only three additional ones, on samples collected at Stations 1, 2, and 5.

The elemental compositions obtained by means of X-ray fluorescence (XRF) appear in **Table 2**. Their basic composition is readily appreciated from their low silica content. After data normalization, the results were processed with the IGPET version 2005 software [9] to get the total alkali silica (TAS; [10]) and Alkali FeOMgO (AFM; [11]) diagrams are shown in **Figures 18** and **19**. Results are quite similar to the elemental data for the ten whole-rock samples across the island reported in [1].

Component	ISA-01	ISA-02	ISA-05
SiO ₂	46.421	43.146	47.316
TiO ₂	1.456	1.566	1.508
Al ₂ O ₃	14.64	15.34	15.35
Fe ₂ O _{3t}	9.357	9.315	9.052
MnO	0.159	0.15	0.15
MgO	10.107	9.226	10.06
CaO	11.25	10.108	9.869
Na ₂ O	2.749	3.283	3.172
K ₂ O	1.341	1.501	1.526
P ₂ O ₅	1.056	1.671	0.856
PXC	1.36	1.59	1.04
Total	99.896	96.896	99.899

Table 2. Elemental composition of three samples from Isla Isabel from X-ray fluorescence (wt%); they correspond to basalt.

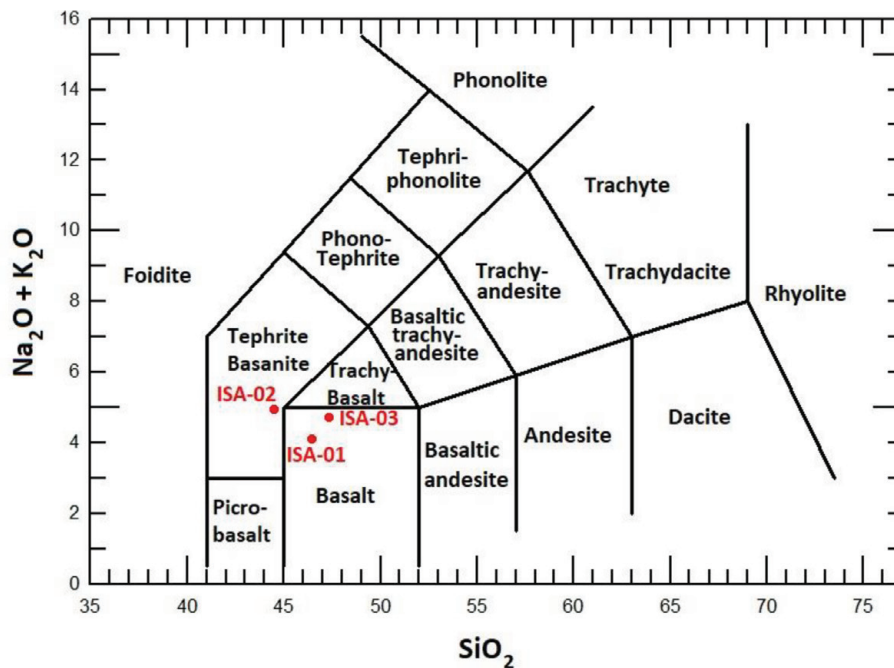


Figure 18. Total alkali silica (TAS) diagram of samples ISA-01-03 (red) classified as basalt and tephrite-basanite from the elemental compositions in **Table 2**.

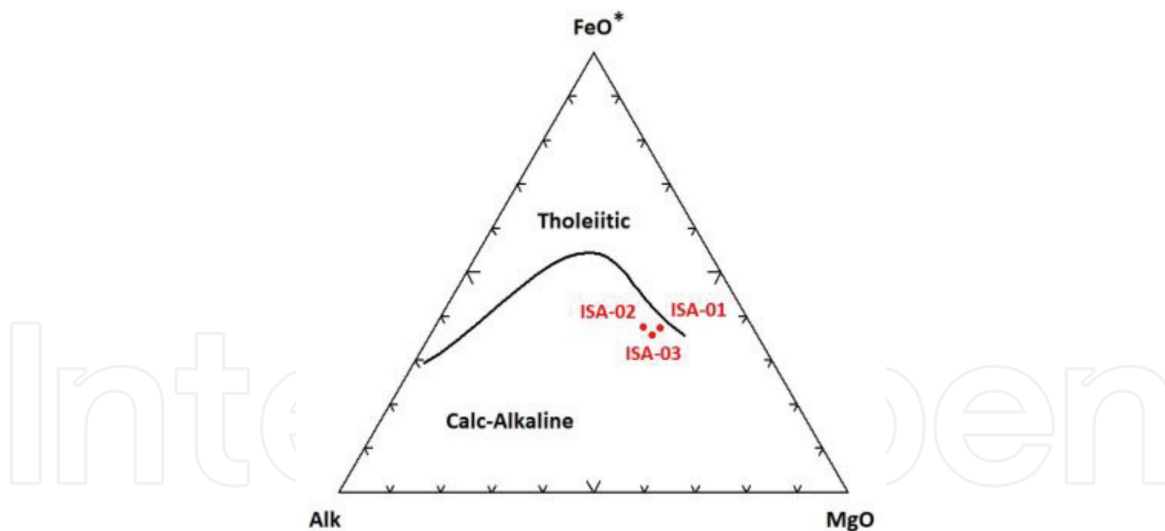


Figure 19. Alkali FeOMgO (AFM) diagram of samples ISA-01-03 (red) from the elemental compositions in **Table 2**.

Mineral content of basalts: groundmass generally of pyroxene (augite), plagioclase and olivine, possibly with minor glass; if porphyritic, the phenocrysts will be any of olivine, pyroxene or plagioclase. Silica (SiO_2) content—45–52%.

5. Mapping hydrothermal alterations

The date of **Figure 2** corresponds to the dry season, where vegetation influence is minimized; the scene is devoid of clouds. Landsat 8 images contain 11 bands; in this processing, we used coastal/aerosol, blue, green, red, NIR, and 2 of the SWIR bands [12].

Atmospheric correction was performed with the Histogram Minimum Method (e.g., [13]). The radiometric correction was performed resampling the image's digital numbers to fit the 8-bit radiometric resolution; the spatial resolution was not modified. The image with these corrections was presented above in **Figure 2**.

To map regions of hydrothermal alteration, we focus on enhancing the spectral response of their typical mineralogical contents. Three major groups characterize hydrothermal alterations (e.g., [14]), hydroxyls (clays and micas), iron minerals (hematite, goethite, and jarosite), and hydrated sulfates (chalk and alunite). Their spectral signatures appear in **Figure 20**.

The identification of hydrothermal alterations is approached with four methods, to be discussed below, applied to the satellite image: Band Ratio, Principal Component Analysis (PCA), the Crosta Technique (Crosta), and the Fraser Technique (Fraser). Results are compared and discussed to optimize the hydrothermal identification.

5.1 Band ratio

Enhancement of hydrothermal alterations is performed making the ratio of the satellite bands that better characterize them. Bands B4/B2 for the oxides, and bands B6/B7 for the hydroxyls. The ratio B5/B4 is included to represent vegetation in the color composition representation of these components, as shown in **Figure 21**.

The digital numbers resulting from the band ratios are rescaled to cover the digital values from 0 to 255 for each ratio. A better visualization is obtained when the false color image is classified; we obtain the percentage of pixels belonging to each class: oxides, hydroxyls, and vegetation, as well as their combinations, and a marine water class, which define eight classes. K-means clustering [16] was used to partition the n-observations into k-clusters, in which each observation belongs to

the cluster with the nearest mean, resulting in a prototype of the cluster. The result of applying this algorithm to the image in **Figure 21** is shown in **Figure 22**, where the classes have been color coded.

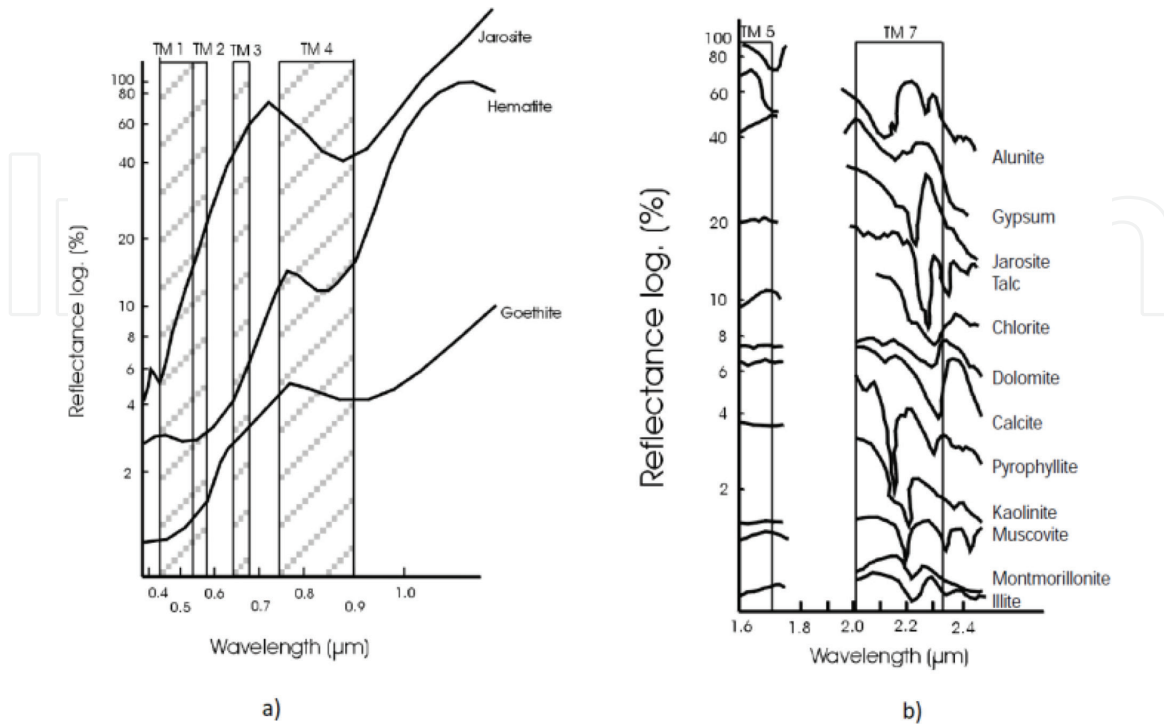


Figure 20. Spectral signatures of hydrothermal alteration minerals. (a) Oxides and (b) hydroxyls. Adapted from [15].

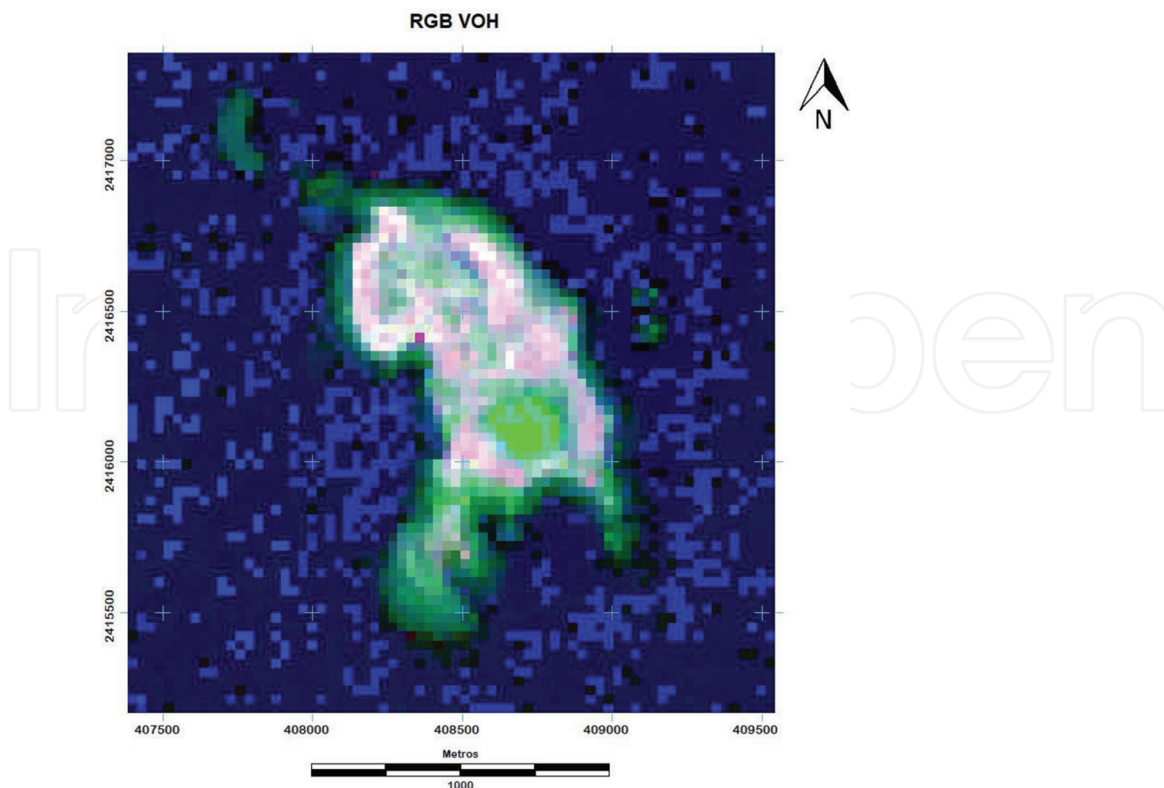


Figure 21. RGB composition of the band ratio process: vegetation (B_5/B_4 , red), oxides (B_4/B_2 , green), and hydroxyls (B_6/B_7 , blue). Vegetation pixels and oxide pixels are abundant, while a few cyan colors are observed, which represent the combined response of oxides and hydroxyls to hydrothermal alterations. The fuzzy appearance is due to the scale used, which begins to show individual pixels.

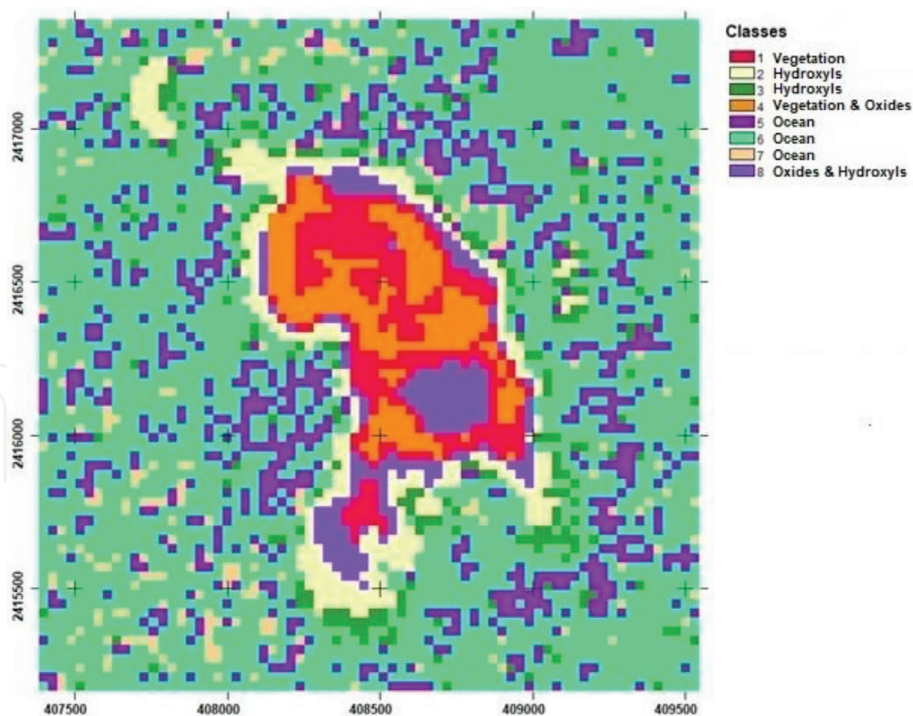


Figure 22. Classification resulting of applying the K-means algorithm to the band ratio and RGB image in **Figure 21**.

Type	Number of pixels	Class
Ocean	3992	5–7
Vegetation	—	—
Oxides	—	—
Hydroxyls	562	2, 3
Vegetation & oxides	508	4
Vegetation & hydroxyls	271	1
Oxides & hydroxyls	194	8

Table 3. Type, class, and the number of pixels in each class in the classified image of **Figure 22**, obtained with the command “Area” in IDRISI.

As can be appreciated from these results, oxides and hydroxyls (Class 8) are confused with the water of Lago Crater. From **Table 3**, we can see no pixels associated with vegetation or oxides, indicating the need for a better class identification scheme.

5.2 Principal component analysis

Principal component analysis (PCA) is a procedure to decorrelate a set of original variables by means of orthogonal transformations [17]. The principal components are linear combinations of the original variables, and it is expected that only the first ones contain the largest variability, obtaining a decrement in the data dimensions. IDRISI [18] contains a module to calculate the resulting matrix; each band of the cropped image (**Figure 2**) is loaded into the program. **Table 4** shows the result of the calculation. As an example of the use of the matrix, we recall the band ratio for the oxides: B4/B2. Across B2 and B4, we select the two most distant values from zero value (positive and negative), finding this condition in C4, B2, and B4; thus $\{B4/B2\} = 0.100/-0.159$. For hydroxyls, we used band ratio B6/B7, finding the above

	C1	C2	C3	C4	C5	C6	C7
B1	0.256965	0.887104	-0.348040	-0.138155	0.059819	-0.008275	0.056119
B2	0.306908	0.876144	-0.333635	<u>-0.159081</u>	0.011407	0.009315	0.036665
B3	0.647203	0.710474	-0.245058	0.054281	-0.115471	0.000692	0.004537
B4	0.662972	0.731901	-0.096873	<u>0.100614</u>	0.072249	-0.006020	-0.005010
B5	0.989940	-0.129653	-0.056608	0.000090	0.001800	0.000952	0.000014
B6	0.958162	0.191692	0.211512	-0.014765	-0.006699	<u>-0.013415</u>	-0.000511
B7	0.904145	0.324699	0.273529	-0.000734	0.0028420	<u>0.047437</u>	0.003909

Rows show the original bands and columns show the principal components. Blue, green, and red identify selections.

Table 4.
Weight matrix of the principal component analysis.

Type	Number of pixels	Class
Ocean	4241	5, 7
Vegetation	238	1
Oxides	197	2, 4
Hydroxyls	238	3
Vegetation & oxides	—	—
Vegetation & hydroxyls	215	8
Oxides & hydroxyls	127	6

Table 5.
Classification of pixel type obtained with the K-means algorithm for the PCA.

condition along C6. This criterion is not fulfilled for the ratio B5/B4 representing vegetation; to obtain a false color image for PCA, we introduce it separately.

A PCA representation of vegetation, oxides, and hydroxyls (RGB) similar to that in **Figure 22** is obtained (not shown). The K-means algorithm was also applied to that image, and the results appear in **Table 5**. Vegetation and oxide pixels are now present although the combined vegetation & oxides class could not locate any. The ocean classes show a new, large area NE of the island that is tentatively identified with the existence of basalt flows at the shallow ocean bottom. The classification result is shown in **Figure 23**.

5.3 Crosta technique

A variant of the PCA is the oriented principal components (OPC), also known as the Crosta Technique [19]. This technique consists of subjecting the specific bands of a given type, and bands not associated with it, to a PCA. A new PCA was calculated with the bands representative of vegetation (B4 and B5) and the band showing the least possible correlation, which in this case is Band 7. **Table 6** is similar to **Table 4**, but with only three components; the band ratio (B5/B4) can be

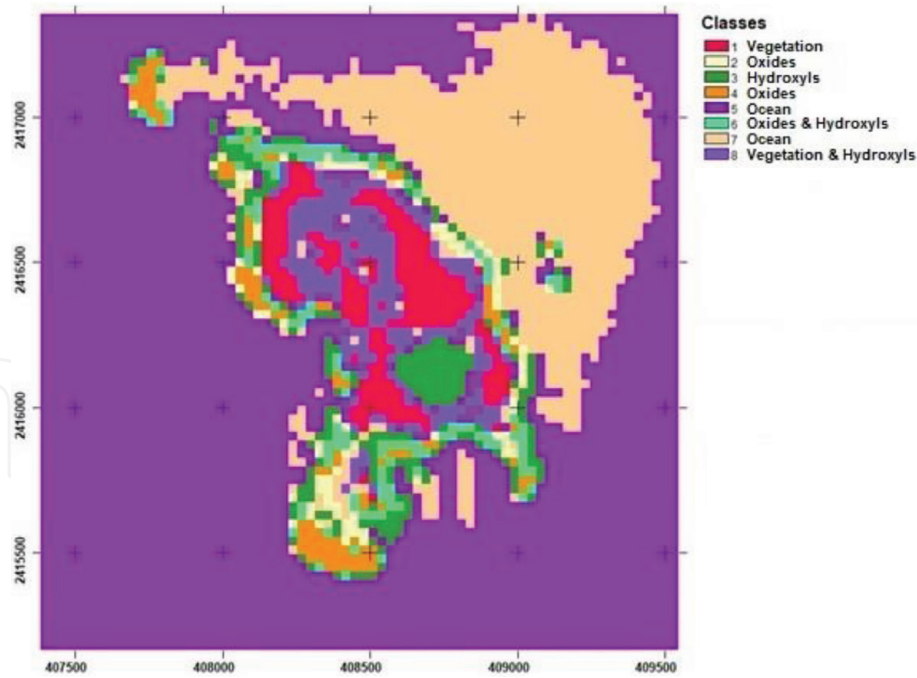


Figure 23.
 The K-means algorithm was applied to the PCA. The class ocean (light brown) is observed near shore and at a large lobe on the NE portion of the figure corresponding to the rim of the island where basalts are exposed at the shallow bottom.

	C1	C2	C3
B4	0.606464	0.863104	0.168687
B5	0.998631	-0.051582	0.008732
B7	0.863104	0.427635	-0.268663

Table 6.
 Weight matrix for the Crosta technique applied to vegetation.

	C1	C2	C3	C4
B2	0.254797	0.902392	0.31147	0.154124
B4	0.610726	0.785016	0.040743	-0.095410
B5	0.998373	-0.055148	0.014464	0.000033
B7	0.864659	0.381888	-0.323275	0.044944

Table 7.
 Weight matrix for the Crosta technique applied to oxides.

	C1	C2	C3	C4
B2	0.26655	0.660609	0.701797	-0.005234
B5	0.99402	-0.107101	0.021272	0.001074
B6	0.95101	0.297992	-0.080951	-0.015088
B7	0.891873	0.441765	-0.082842	0.050436

Table 8.
 Weight matrix for the Crosta technique applied to hydroxyls.

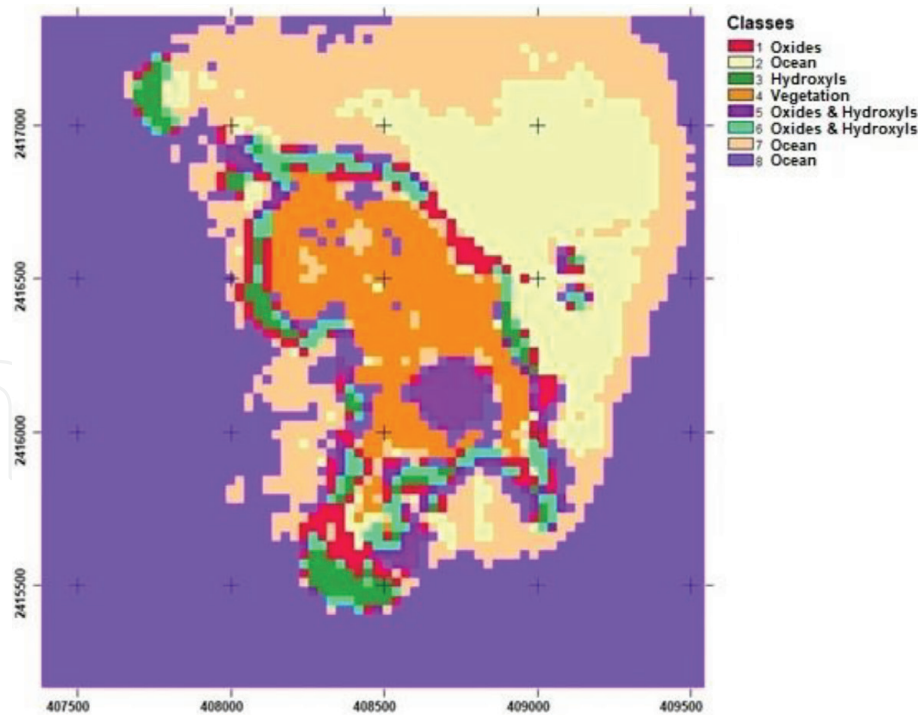


Figure 24. The K-means algorithm was applied to the results of the Crosta calculation to obtain the number of pixels in each type. Two classes of ocean pixels are distinguished here, the one with the lighter tone corresponding better with the area of the clearly visible submerged basalts.

Type	Number of pixels	Class
Ocean	4332	2, 7, 8
Vegetation	396	4
Oxides	176	1
Hydroxyls	96	3
Vegetation & oxides	—	—
Vegetation & hydroxyls	—	—
Oxides & hydroxyls	256	5, 6

Table 9. Classification of pixel type obtained with the K-means algorithm for the PCA of the Crosta technique results (Table 6).

obtained from column C2. Additionally, two independent analyses are performed for oxides and hydroxyls; for oxides, we take bands 2, 4, 5, and 7 to avoid mapping hydroxyls. The corresponding weight matrix appears in Table 7. For the hydroxyls, we used bands 2, 5, 6, and 7 to avoid mapping oxides. The corresponding weight matrix is shown in Table 8.

A RGB color composition can now be made with the principal components that represent hydroxyls, oxides, and vegetation (not shown), as previously done with the band ratios in Figure 24. The K-means algorithm was applied to it; the result is shown in Table 9.

Pixel identification resulting from the Crosta Technique for vegetation and the PCA results for oxides and hydroxyls show that hydroxyl identification improved with respect to the PCA results. We applied the K-means algorithm to this procedure to define the number of pixels that correspond to each type. Results appear in Table 9 and Figure 24. This result shows class ocean (light brown) mainly

around the island and in a large lobe NE of the island, interpreted as shallow-depth (≤ 10 m) regions that contain visible basalt flows at the bottom. With this algorithm, we obtained a larger number of pixels of oxides and hydroxyls than those obtained with the band ratio method. However, it still cannot properly identify regions of vegetation with oxides or hydroxyls.

Although this is an improved version of the band ratio method, we also observe that the Crosta algorithm has not been able to fully identify the different pixel types, as shown in **Table 7**. Nonetheless, this algorithm shows improvements with respect to the former since it has distinguished more pixels of the oxide-hydroxyl mixture (Classes 5, 6), which is the objective of this work. Additionally, it shows some yellow pixels representing the mixed type of oxides and vegetation, only present in the band ratio and in the Fraser technique, to be discussed later.

5.4 Fraser technique

This technique uses input bands as the band ratios that highlight the spectral characteristics of the materials of interest [20]. The idea is to separate the spectral differences of the materials, accomplished via the two resulting eigen vectors. In this process, a PCA analysis must be performed twice, one involves the band ratio

	C1	C2
Vegetation	0.982941	-0.183921
Oxides	0.890346	0.455285

Table 10.
 Weight matrix for the Fraser technique applied to vegetation and oxides.

	C1	C2
Vegetation	0.986763	-0.162172
Oxides	0.708288	0.705924

Table 11.
 Weight matrix for the Fraser technique applied to vegetation and hydroxyls.

for vegetation and the band ratio for the oxides. The second involves the band ratio for vegetation and the band ratio for hydroxyls. **Tables 10** and **11** show the corresponding results. To continue with the analysis, the associated RGB color composition image was prepared (**Figure 25**). Subsequently, the K-means algorithm is applied to the RGB color composition of the Fraser technique (**Figure 26**).

5.5 Lineament extraction

In geological structures, surface lineaments are often generated by deeply seated processes; such is often the case of faults and some mineral deposits. From satellite images, one can extract surface lineaments that may be associated with a given problem. In the present case, we can explore the association between surface lineaments and the hydrothermal alterations already mapped. To this end, we used Band 6 of the cropped Landsat image (**Figure 2**) and applied the four directional filters: N-S, E-W, NE-SW, and NW-SE, which represent the Freeman Code of Eight Directions (FCCE) [21]. The traces of the obtained lineaments are superposed to

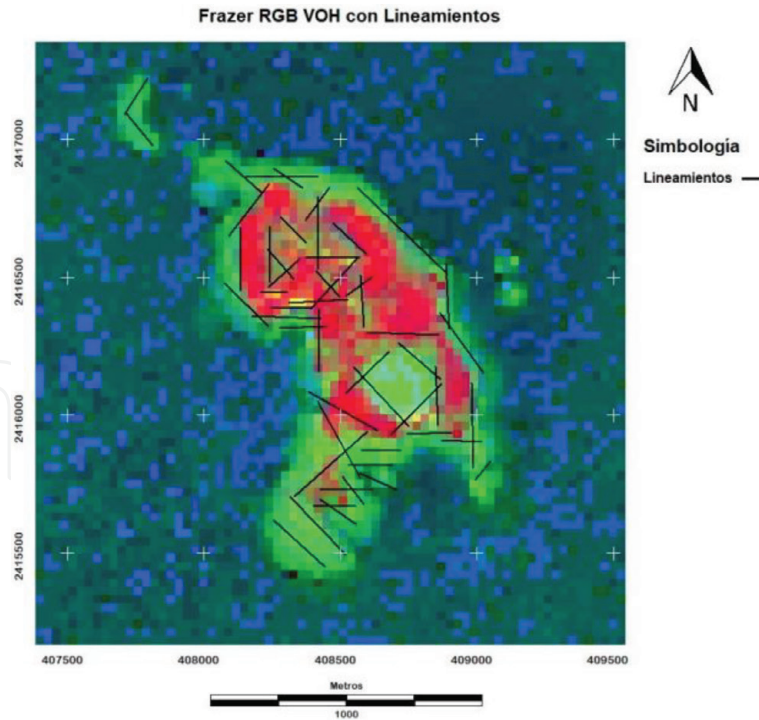


Figure 25. RGB color composition image for the Fraser technique: vegetation (red), oxides (green), and hydroxyls (blue) including a set of lineaments (black lines) obtained from band 6 of the image, by means of directional filters.

Type	Number of pixels	Class
Ocean	3298	2, 4, 6
Vegetation	—	—
Oxides	—	—
Hydroxyls	963	7
Vegetation & oxides	197	5
Vegetation & hydroxyls	251	3
Oxides & hydroxyls	547	1, 8

Table 12. The K-means algorithm is applied to the color composite image of the Fraser technique (Figure 25).

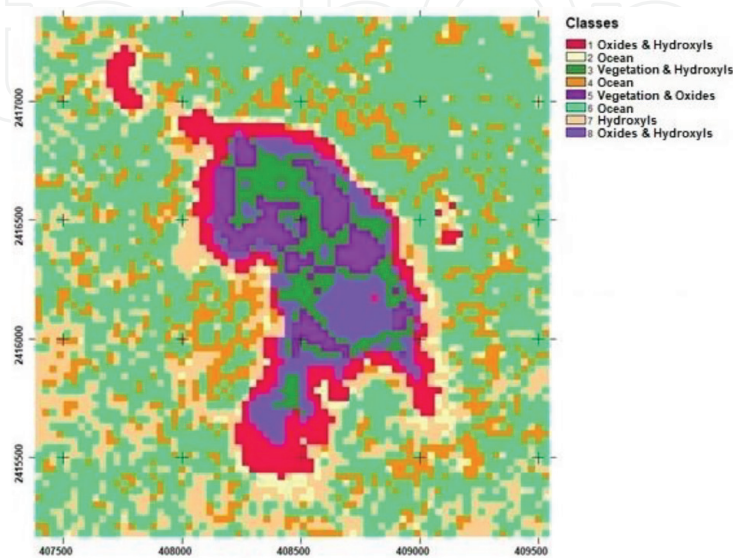


Figure 26. The K-means algorithm is applied to the RGB color composition image of the Fraser technique (Figure 25), with the indicated classes. Table 12 shows the number of pixels identified in each class.

the RGB color composition of the Fraser technique in **Figure 25**. A tendency is observed for the lineaments to follow a predominantly NW-SE direction, aligned with the main body of the island and with the orientation of the underlying laccolith [2], as well as with the main alignment of reported explosion craters [1]. The residual Bouguer anomaly of the island [3] also follows this direction suggesting that regional tectonic mechanisms favor this orientation. A more comprehensive discussion of the relation between lineaments and geophysical properties is beyond the scope of this study.

6. Conclusions

In summary, the comparison of these classifications: band ratio, PCA, Crosta, and Fraser techniques illustrates the difficulties and variants inherent in these classification methods. No single procedure appears to optimize all the parameters of interest. This set exemplifies potential variants in field explorations and shows the path for choosing the best alternative, or combination thereof, of interpretation for the problem at hand. For instance, the Fraser technique succeeded in identifying basalt flows covered by vegetation in the north half of the island but failed to locate the submerged basalts that were identified with the Crosta technique. In turn, the latter failed to identify the basalts covered by vegetation. Hydrothermal alterations are identified with different degrees of precision, indicating that if such is the target, one should evaluate various alternatives to optimize results. The analysis of the lineaments in the island, easily obtained by remote sensing, is associated with surface geological features and deep geophysical properties. They should be incorporated as frequently as possible into this type of studies.

The presence of hydrothermal activity in Isla Isabel extends almost fully throughout the island. Detection of such an activity under vegetated areas shows now that the northern half of the island is also the site of extended alterations. The possibility of basalt flooding in this region is high, and it should be the subject of detailed mapping. The high heat flow in the area, the existence of a laccolith under Isla Isabel, the extensive phreatomagmatic activity, and the presence of hydrothermal alterations in the island point to the relevance of this region as a potential geothermal source of major importance.

Acknowledgements

We acknowledge the expedient processing of permits to access the National Park by J. Castrejón, Director of Parque Nacional Isla Isabel. R. Lozano performed the geochemistry analyses in the X-ray Fluorescence Laboratory, his contribution is greatly appreciated.

IntechOpen

Author details

Román Alvarez^{1*} and Gerardo Figueroa²

1 Institute of Applied Mathematics (IIMAS), National University of Mexico (UNAM), Mexico City, Mexico

2 Earth Sciences Department, National University of Mexico (UNAM), Mexico City, Mexico

*Address all correspondence to: roman.alvarez@iimas.unam.mx

IntechOpen

© 2018 The Author(s). Licensee IntechOpen. This chapter is distributed under the terms of the Creative Commons Attribution License (<http://creativecommons.org/licenses/by/3.0>), which permits unrestricted use, distribution, and reproduction in any medium, provided the original work is properly cited. 

References

- [1] Housh TB, Aranda-Gómez JJ, Luhr JF. Isla Isabel (Nayarit, México): Quaternary basalts with mantle xenoliths erupted in the mouth of the Gulf of California. *Journal of Volcanology and Geothermal Research*. 2009;197:85-107. DOI: 10.1016/j.jvolgeores.2009.06.011
- [2] Alvarez R, Camargo FC, Yutsis V, Arzate J. A volcanic centre in Mexico's Pacific continental shelf. In: Németh K, Carrasco-Núñez G, Aranda-Gómez JJ, Smith IEM, editors. *Monogenetic Volcanism*. London. Special Publications 446: Geological Society; 2017. DOI: 10.1144/SP446.12
- [3] Alvarez R, Camargo FC, Yutsis VV. Geophysical modelling of Isla Isabel: A volcanic island on the Mexican continental margin. In: Németh K, Carrasco-Núñez G, Aranda-Gómez JJ, Smith IEM, editors. *Monogenetic Volcanism*. London. Special Publications 446: Geological Society; 2017. DOI: 10.1144/SP446.13
- [4] Reyes-Flores R. Petroleum exploration in the Pacific continental platform (states of Nayarit and Sinaloa). *Ingeniería Petrolera*. 1983;5-20. In Spanish
- [5] Clark RN. USGS Spectroscopy Lab. <https://speclab.cr.usgs.gov/>
- [6] Remote Sensing & GIS. Elementary Atmospheric Correction for Landsat Images: Haze Correction via Histogram Minimum. 2015. <https://scientiaplusconscientia.worldpress.com>
- [7] Huang CP, Lavenburg G. Impacts of Bird Droppings and Deicing Salts on Highway Structures: Monitoring, Diagnosis, Prevention. Newark, Delaware: Civil and Environmental Engineering, University of Delaware; 2011
- [8] Jensen JR. *Remote Sensing of Environment*. 2nd ed. London: Pearson Prentice Hall; 2007
- [9] Available from: <https://www.scribd.com/doc/162902456/Igpet-Manual>
- [10] Le Bas MJ, Le Maitre RW, Streckeisen A, Zanettin B. A chemical classification of volcanic rocks based on the total alkali silica diagram. *Journal of Petrology*. 1986;27:745-750
- [11] Irvine TN, Baragar WR. A guide to the chemical classification of the common volcanic rocks. *Canadian Journal of Earth Sciences*. 1971;8:523-548
- [12] Zanter K. *Landsat 8 Data User Handbook*. Sioux Falls, South Dakota: Department of the Interior U.S. Geological Survey; 2016
- [13] Intel Corporation. *Open Source Computer Vision Library Reference Manual (PDF)*. 2001
- [14] Ruiz-Armenta JR, Prol-Ledesma RM. Image processing techniques for the exploration of ore minerals of hydrothermal origin. *Física de la Tierra*. 1995;7:105-137. In Spanish
- [15] de la Vega-Márquez TF, Prol-Ledesma RM, Orozco G. Hydrothermal alteration and main structures mapping using TM images in La primavera geothermal field (Mexico). *Geofísica Internacional*. 2001;40:147-162
- [16] Hartigan JA, Wong MA. Algorithm AS 136: A K-means clustering algorithm. *Journal of the Royal Statistical Society: Series C (Applied Statistics)*. 1979;28(1):100-108. DOI: 10.2307/234683
- [17] Abdi H, Williams LJ. *Principal component analysis*. Wiley Interdisciplinary Reviews:

Computational Statistics.
2010;2(4):433-459. DOI: 10.1002/
wics.101

[18] IDRISI. [https://clarklabs.org/terrset/
idrisi-gis](https://clarklabs.org/terrset/idrisi-gis)

[19] Lei L, Da-Fang Z, Jun Z,
Dong-Sheng Q. Alteration mineral
mapping using masking and Crosta
technique for mineral exploration
in mid-vegetated areas: A case study
in Areletuobie, Xinjiang (China).
International Journal of Remote
Sensing. 2011;32(7):1931-1944.
DOI: 10.1080/01431161003639678

[20] Fraser SJ. Discrimination and
identification of ferric oxides using
satellite thematic mapper data: A
newman case study. International
Journal of Remote Sensing.
1991;12:635-641

[21] Freeman H. On the encoding of
arbitrary geometric configurations. IRE
Transactions on Electronic Computers.
1961;EC-10:260-268